Comparative study of the luminescence properties of Er-, Nd- and Tm-doped Si–ZrO_2 co-sputtered films

2008 J. Phys.: Condens. Matter 20 315003

(http://iopscience.iop.org/0953-8984/20/31/315003)

J. Phys.: Condens. Matter **20** (2008) 315003 (7pp) doi:10.1088/0953-8984/20/31/315003

Comparative study of the luminescence properties of Er-, Nd- and Tm-doped Si–ZrO_2 CO-sputtered films

C Rozo and L F Fonseca

Physics Department and Institute for Functional Nanomaterials, University of Puerto Rico at Río Piedras, USA

Received 13 December 2007, in final form 28 March 2008
Published 26 June 2008
Online at stacks.iop.org/JPhysCM/20/315003

Abstract

Er-, Nd- and Tm-doped Si-yttria stabilized zirconia (YSZ) thin film samples were prepared by rf co-sputtering. Chemical composition of the samples was determined using energy-dispersive spectroscopy (EDS) and the structure of the films by x-ray diffraction (XRD). The samples were annealed to 700 °C. Photoluminescence (PL) measurements were performed for the visible and infrared. Excitation with 457.9 nm produces spectra in the visible range due mostly to defects in the YSZ matrix with a weak Si nanoparticle surface state emission; the Tm-doped samples also present Tm^{3+}:$^3H_4 \rightarrow {}^3H_6$ emission. Excitation with 488 nm produces spectra in the visible range with additional rare earth emissions such as the Er^{3+}:$^2H_{11/2} \rightarrow {}^4I_{15/2}$, $^4S_{3/2} \rightarrow {}^4I_{15/2}$ and $^4F_{9/2} \rightarrow {}^4I_{15/2}$ emissions for the Er-doped samples and the Nd^{3+}:($^4F_{5/2}$,$^2H_{9/2}$) $\rightarrow {}^4I_{9/2}$ emissions for the Nd-doped samples. The Er-doped samples present weak Er^{3+}:$^4I_{11/2} \rightarrow {}^4I_{15/2}$ emissions and narrow Er^{3+}:$^4I_{13/2} \rightarrow {}^4I_{15/2}$ emissions in the infrared range, while the Nd-doped samples present Nd^{3+}:$^4F_{3/2} \rightarrow {}^4I_{9/2}$, $^4F_{3/2} \rightarrow {}^4I_{11/2}$ and $^4F_{3/2} \rightarrow {}^4I_{13/2}$ emissions. No Tm^{3+} emissions in the infrared were observed. Excitation wavelength dependence measurements for the Er^{3+}:$^4I_{13/2} \rightarrow {}^4I_{15/2}$ emissions show that these are due to energy transfer from the defects in the YSZ as well as from the Si nanoparticles while the same measurements for the Nd^{3+}:$^4F_{3/2} \rightarrow {}^4I_{11/2}$ emissions show that these are due to energy transfer from the Si nanoparticles only. Excitation flux dependence measurements for the Er^{3+}:$^4I_{13/2} \rightarrow {}^4I_{15/2}$ and Nd^{3+}:$^4F_{3/2} \rightarrow {}^4I_{11/2}$ emissions show the sub-linear dependence characteristic of rare earth ion excitation through energy transfer from Si nanoparticles. Er^{3+}:$^4I_{11/2} \rightarrow {}^4I_{15/2}$ emission dependence on Er^{3+}:$^4I_{13/2} \rightarrow {}^4I_{15/2}$ emission showed that the former was possibly due to a combination of downconversion from higher levels of the Er ions, energy transfer from Si nanoparticles and upconversion transfer processes.

We concluded that Er-, Nd- and Tm-doped Si-YSZ are promising materials for photonic applications, being easily broadband excited using low pumping powers.

1. Introduction

Zirconium oxide has been proposed as an excellent material for optical applications due to its hardness, high optical transparency in the 0.3–8 μm range and high refractive index [1, 2]. With a wide optical bandgap of 5.22–5.8 eV [3], which reduces the probability of non-radiative decay, and with a low phonon energy (470 cm^{-1}), lower than that of SiO_2 (1100 cm^{-1}) and of Al_2O_3 (870 cm^{-1}) [4], which reduces the probability of phonon-assisted non-radiative relaxation, the number and probability of radiative transitions in rare earth doped ZrO_2 increases, which has made such rare earth (RE) doped oxides interesting for photonic applications. Luminescence in Pr^{3+}-, Tb^{3+}-, Eu^{3+}-, Sm^{3+}- and Er^{3+}-doped ZrO_2 (bulk, powders, nanocrystals or sol–gel) have been investigated [5–10]. Er-doped waveguides and LEDs have also been developed [11, 12].

ZrO_2 crystallizes into three main phases: the monoclinic, tetragonal and cubic. The monoclinic (m) phase is thermodynamically stable for temperatures below 1170 °C. From 1170 to 2370 °C ZrO_2 is tetragonal (t), while above 2370 °C ZrO_2 is cubic (c) until it melts at 2706 °C [13]. The

Table 1. Chemical composition of rare-earth-doped film samples.

Film sample reference	Zr (at.%)	Y (at.%)	O (at.%)	Si (at.%)	RE (at.%)
B4	—	—	57.93	41.65	(Er) 0.42
D4	—	—	58.58	41.06	(Nd) 0.36
F2	31.27	4.05	60.18	3.65	(Er) 0.85
F3	31.79	4.00	59.05	4.09	(Er) 1.07
H3	28.83	3.78	61.72	3.83	(Nd) 1.85
H4	28.10	3.74	61.55	5.36	(Nd) 1.26
J2	30.27	6.31	55.29	6.63	(Tm) 1.51
J3	28.10	5.65	55.48	9.71	(Tm) 1.05

tetragonal phase is stabilized at relatively low temperatures by the addition of dopants such as Er^{3+}, Y^{3+} and Ca^{2+} cations [4]. The cubic phase can be stabilized at low temperatures by the addition of substitutional cations, such as Ca^{2+}, Mg^{2+} and Y^{3+} [14]. Y_2O_3 is used to stabilize the tetragonal (t) and cubic (c) phases of yttria-stabilized zirconia (YSZ) over the composition ranges 2–9 mol% and 4–40 mol% of Y_2O_3. The Y^{3+} dopants substitute for the host cations and, to preserve charge neutrality, one O vacancy V^0 must be created for each pair of dopant cations. In YSZ local atomic environments differ from stoichiometric high temperature t- and c-phases of pure ZrO_2 due to the presence of relaxed defects. The average cation coordination number (7–8) is reduced gradually with increasing Y_2O_3 [15]. YSZ ($(ZrO_2)_{1-x}(Y_2O_3)_x$) has the CaF_2 cubic structure for a wide range of values of x. Oxygen vacancies result in departures from the fluorite-type lattice. Oxygen coordination around active impurities can be sixfold, sevenfold or eightfold for Eu^{3+}- and Er^{3+}-doped YSZ [16]. Nd^{3+} can only be incorporated in sevenfold configurations [16].

Nd-, Er- and Tm-doped silicon-rich silicon oxide (SRSO) films present IR PL emissions at 0.92 μm, and 1.10 μm (Nd), at 0.98 μm and 1.54 μm (Er), and at 1.65 μm (Tm), respectively, with the advantage of being able to be pumped with low power sources, including inexpensive visible laser diodes and broad band sources such as visible LEDs [17–19]. The high absorption cross sections and broadband absorption in the visible range of the Si nanoparticles (np) allow them to be efficient sensitizers to enhance these RE^{3+} emissions [18–20]. It is then of great interest from both scientific and technological points of view to investigate the spectroscopic properties of Si np-sensitized RE^{3+} emissions in YSZ films for photonic applications. This paper presents a comparative study of the optical properties of such nanocomposites with Er, Nd or Tm as dopants and evaluates their potential for applications.

2. Experimental details

RE_2O_3-Si-YSZ (RE = Er, Nd, Tm) film samples were prepared by non-reactive rf sputtering. The YSZ target (ZrO_2+ 12 wt% Y_2O_3) has an area of 181.46 cm^2. The RE_2O_3 target area used was 1.43 cm^2; the Si target area used was 6.67 cm^2. The RE_2O_3/Si (RE = Er, Nd, Tm) area ratio was 0.214 and the Si/YSZ area ratio was 0.037. The target–substrate distance is ∼2.54 cm. The deposition time was 6 h, the power used ∼200 W, the chamber pressure during deposition ∼0.1 Torr, the argon pressure ∼20 mTorr, the chamber residual pressure $\sim 5.0 \times 10^{-7}$ Torr and the deposition temperature ∼125 °C. Fused silica substrates were used. Film chemical composition was determined using a JEOL JSM-5800LV SEM equipped with EDAX®. Film thickness was measured for the as-deposited films using a Dektak Profilometer. The thickness of the film samples varies from 2 to 4 μm. The film samples were annealed to 700 °C for a 30 min stay, with a mean heating rate of 10.8 °C min^{-1} and a mean cooling rate of 2.4 °C min^{-1}. The film samples were characterized by x-ray diffraction using Siemens D-5000 equipment. Photoluminescence measurements in the visible and the infrared were performed at room temperature using an Ar laser, an ISA-TRIAX 320 spectrometer equipped with a Hamamatsu R2949 photomultiplier (PMT) and an InGaAs detector connected to a lock-in amplifier.

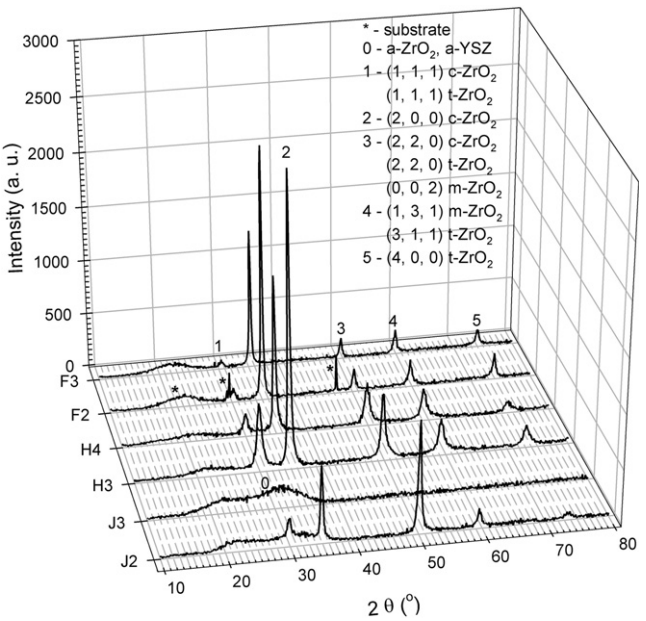

Figure 1. XRD patterns rare-earth-doped YSZ films annealed to 700 °C.

3. Results and discussion

Chemical composition of the film samples is shown in table 1. For most of the film samples the RE content is relatively high, being greater than 1.0 at.% (10 000 ppm). In the case of most commercial Er-doped optical amplifier fibers the Er content does not exceed 1000 ppm to avoid concentration quenching effects [21]. XRD patterns for the film samples presented in table 1 annealed to 700 °C are presented in figure 1. The peaks or bands labeled with asterisks correspond to the fused silica substrate. The peaks numbered from 1 to 5 were identified as being of crystalline ZrO_2 phases (tetragonal (t-), cubic (c-), and monoclinic (m-)) and the band numbered with a 0 corresponds to amorphous ZrO_2 or amorphous YSZ. The c-ZrO_2 phase seems to be the predominant crystalline phase for the film samples, with the exception of J2. The main crystalline grain

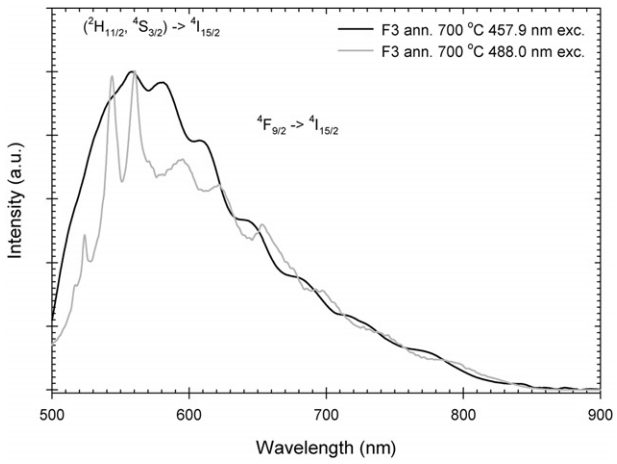

Figure 2. Visible PL spectra for Er-doped YSZ film sample F3 annealed to 700 °C for 488.0 nm excitation and 457.9 nm excitation at 20 mW.

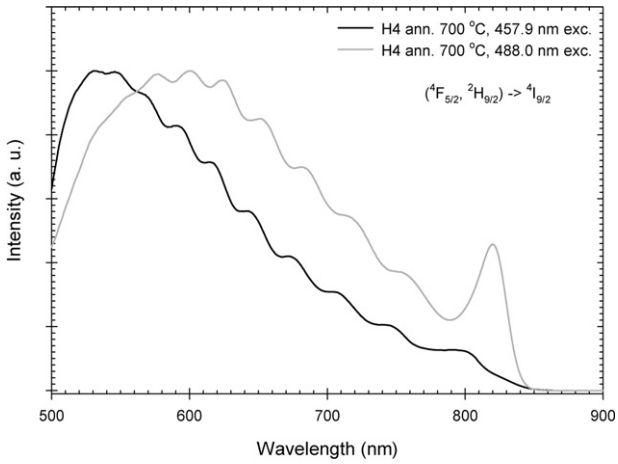

Figure 3. Visible PL spectra for Nd-doped YSZ film sample H4 annealed to 700 °C for 488.0 nm excitation and 457.9 nm excitation at 20 mW.

orientation for J2 also differs from that of the Er- and Nd-doped samples where the orientation mostly corresponds to the [2, 0, 0] and [2, 2, 0] directions. The peaks associated with the crystalline ZrO_2 phases decrease with the increase in Si content and for Si content beyond 9.0 at.% the film samples can become amorphous, as is the case with sample J3. Sample J2 has Si content high enough for amorphous ZrO_2 or amorphous YSZ to be present in the film sample. The main crystalline grain orientation also changes for high Si content, before the samples may become amorphous, as is the case with J2. The relative oxygen deficiency (below 66 at.%) with higher Zr and Y contents could be the reason for the segregation of the crystalline phases. The formation and growth of Si nanoparticles after annealing would disrupt the crystalline lattices, reducing the long-range order of the ZrO_2 crystalline structures leading then to an amorphous film. The overall relative oxygen deficiency in the film samples suggests the high presence of oxygen-related vacancies within the film.

Visible PL spectra for the Er-, Nd- and Tm-doped film samples can be seen in figures 2 (F3), 3 (H4) and 4 (J3). The figures illustrate the spectral differences when exciting with 457.9 nm and 488.0 nm. For excitation with 457.9 nm, the Er-doped samples present emissions related to oxygen vacancy defects or interstitial oxygen defects [2, 14, 22–24] in ZrO_2 or YSZ, and Si=O surface state emissions [25] related to small SiO_x ($x < 2$) regions within the film samples. For excitation with 488.0 nm additional luminescence is observed, related to Er^{3+} emissions in the visible: $^2H_{11/2} \rightarrow {}^4I_{15/2}$, $^4S_{3/2} \rightarrow {}^4I_{15/2}$ and $^4F_{9/2} \rightarrow {}^4I_{15/2}$, which correspond to downconversion PL [26]. The Nd-doped samples present the same characteristics of the Er-doped samples: defect emissions and Si=O surface state emissions for excitation with 457.9 nm and then additional Nd^{3+} emission in the visible: $(^4F_{5/2}, {}^2H_{9/2}) \rightarrow {}^4I_{9/2}$, for excitation with 488.0 nm. The Tm-doped samples present defect and surface state emissions along with Tm^{3+}:$^3H_4 \rightarrow {}^3H_6$ emission for excitation with 457.9 nm with no additional emissions on excitation with 488.0 nm. The bands for Nd- and Tm-doped samples present a small

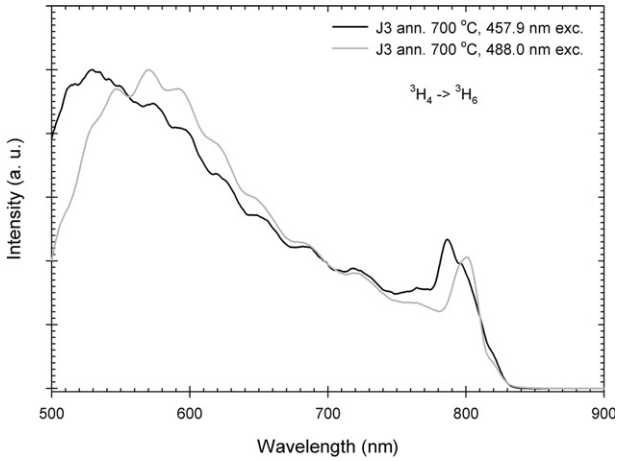

Figure 4. Visible PL spectra for Tm-doped YSZ film sample J3 annealed to 700 °C for 488.0 nm excitation and 457.9 nm excitation at 20 mW.

redshift due to changes in the distribution of de-excitation routes among defects with the change in excitation wavelength which is not visible for Er-doped samples, probably because the Er^{3+} emissions observed lie within the same wavelength range as the defect emissions. The Tm^{3+}:$^3H_4 \rightarrow {}^3H_6$ emission presents a different distribution of transitions among $^3H_4$ and $^3H_6$ sublevels with the change in the excitation wavelength. Interference patterns are observed in the visible PL spectra for the film samples annealed to 700 °C due to changes in the refractive index with annealing.

Figure 5 presents a series of fits performed on the visible spectrum of F3 with the possible emissions for excitation at 457.9 nm. This excitation would excite the observed absorption band in YSZ around 465 nm which corresponds to V-type center (holes trapped at an oxygen ion adjacent to a cation vacancy) defects [23]. Relaxation to several lower levels would produce the observed emissions that compose the spectra produced by excitation at 457.9 nm. The T defects, associated with oxygen vacancies distributed to be

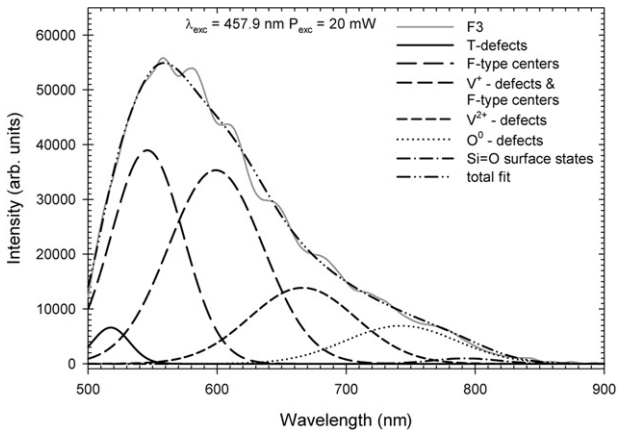

Figure 5. Gaussian fits of the visible spectrum for Er-doped YSZ film sample F3 annealed to 700 °C for 457.9 nm excitation at 20 mW showing components of the visible PL.

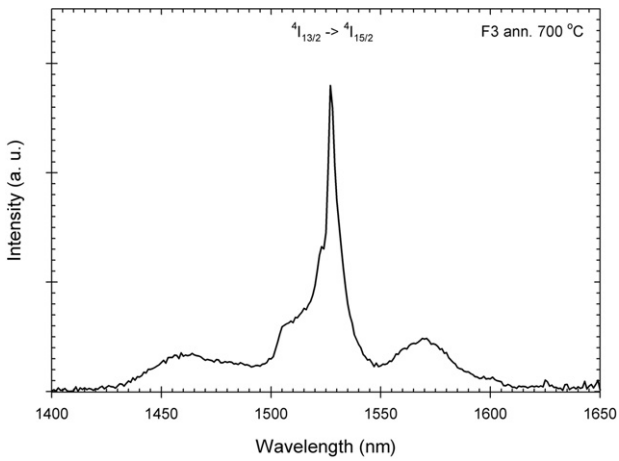

Figure 6. Er^{3+}:$^4I_{13/2} \rightarrow {}^4I_{15/2}$ emission spectrum of Er-doped YSZ film sample F3 annealed to 700 °C for 488 nm excitation at 20 mW.

on opposite cube corners with relaxed oxygens surrounding the vacancies along the [1 0 0] edges, are related to the probable emission corresponding to a transition to the ground state (top of valence band) from a level 2.4 eV above it (peak wavelength of 517 nm) [23]. F-type centers, associated with anion vacancies some of which can have Y^{3+} ions in neighboring positions, act as electron trap defect sites and upon electron–hole recombination at such sites emissions are produced with peak wavelengths of 550 and 600 nm [24]. The positively charged oxygen vacancy V_4^+ is surrounded by four Zr nearest neighbors which are moved apart (0.1 Å) from the vacant site and the remaining electron (related to the vacancy) is strongly localized near the vacant site; upon electron–hole recombination at the site, emission could be produced with peak wavelength 599 nm [22]. The doubly positively charged oxygen vacancy V_4^{2+} is also surrounded by four Zr neighbors but further displaced (an additional 0.1 Å); possible emission related to the vacancy would have a peak wavelength of 667 nm [22]. In the case of the O_3^0 interstitial defect the lattice oxygen relaxes to accommodate the interstitial, distorting the original triple-planar O–Zr_3 group into a slight pyramid with its apex pointing away from the interstitial; possible emission related to the interstitial would have a peak wavelength of 742 nm [22]. The excitation wavelength in this case and the V-type center defect level is not resonant with any Er^{3+} energy level so there is no Er^{3+} ion emission in the visible. In the case of Nd^{3+}, although both the excitation wavelength and the V-type center level correspond to the $^2K_{15/2}$, $^4G_{11/2}$, and $^4G_{9/2}$ levels, the absorption coefficient for these levels is negligible [27, 28] so excitation either through direct optical absorption or through energy transfer from the V-type centers does not take place in H3 and H4.

Excitation at 488.0 nm would excite the observed absorption band in YSZ centered around 480 nm which corresponds to C defects (heptacoordinated Zr^{3+} ions in trigonally distorted cubes that serve as electron traps) [23]. Energy transfer to the Er^{3+}:$^4F_{7/2}$ level in F3 would come from the C defects. The Nd^{3+}:($^4F_{5/2}$, $^2H_{9/2}$) $\rightarrow$ $^4I_{9/2}$ emission may be due to transfer from the lower level T defects, after relaxation from the C-defect levels, to the Nd^{3+}:($^2K_{13/2}$, $^4G_{7/2}$, $^4G_{9/2}$) levels followed by relaxation to the Nd^{3+}:($^4F_{5/2}$, $^2H_{9/2}$) levels. As the Tm^{3+}:$^3H_4 \rightarrow {}^3H_6$ emissions are present for both excitation wavelengths these are then basically due to energy transfer from the Si nanoparticles (from the Si=O surface state levels directly to the Tm^{3+}:$^3H_4$ levels). The only absorbing Tm^{3+} level, $^1G_4$, is not resonant with the excitation wavelengths used or with the main absorbing defect levels. The low-wavelength YSZ defect emissions become weaker with respect to the same emissions in the spectra for 457.9 nm excitation as is shown in figures 2–4.

Figure 6 presents the Er^{3+}:$^4I_{13/2} \rightarrow {}^4I_{15/2}$ emission spectrum peaked at 1527 nm for F3 annealed to 700 °C for a 20 mW 488 nm excitation. This spectrum corresponds to that of Er ions in crystalline environments, with the FWHM varying from 5.0 to 12.0 nm. The polycrystalline nature of the environment in which the Er ions are located is reflected in the relatively broad bandwidth of the $^4I_{13/2} \rightarrow {}^4I_{15/2}$ emission for F3 relative to the bandwidth (1.6 nm) reported for a monocrystalline environment (t-ZrO_2) [11]. This spectral shape can serve for LEDs or laser diodes but not for optical amplifiers, which require greater bandwidth. Figure 7 presents the Nd^{3+}:$^4F_{3/2} \rightarrow {}^4I_{j/2}$; $j = 9, 11, 13$ emissions spectrum peaked at 885 nm, 1060 nm and 1325 nm, respectively, for H4 annealed to 700 °C for a 20 mW 457.9 nm excitation. For comparison purposes the IR spectrum for the Nd-doped Si–SiO_2 film sample D4 (see table 1) is also presented. The H4 Nd^{3+} IR spectrum presents peaks for the 885 nm and 1060 nm emissions that are narrower than for Nd-doped Si-rich SiO_2 films (see figure 7) [29] but are wider than for some Nd-doped bulk glasses [26, 27]. For H4 these bandwidths are 29.0 nm, 34.0 nm and 35.0 nm for the peaks at 885 nm, 1060 nm and 1325 nm, respectively. The peak intensities are in ratios of 1:0.36:0.02 for the peaks at 885 nm, 1060 nm and 1325 nm, respectively, and the integrated intensities are in ratios of 1:0.41:0.02. For optical communications applications corresponding to the O-band the intensity ratios for the $^4F_{3/2} \rightarrow {}^4I_{13/2}$ emission are quite low: however,

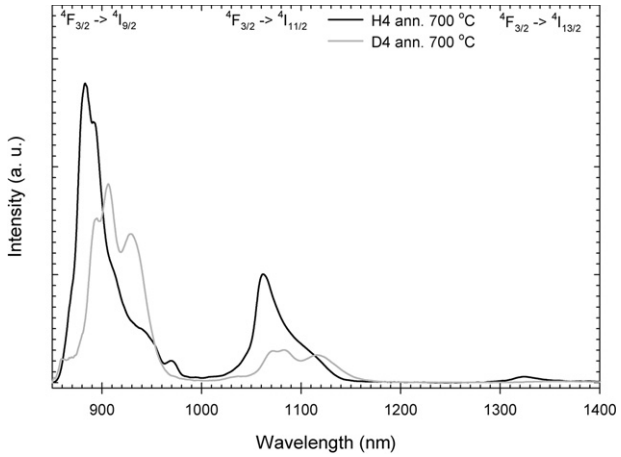

Figure 7. $^4F_{3/2} \rightarrow {}^4I_j$, $j = 9/2, 11/2, 13/2$ emission spectra of Nd-doped YSZ film sample H4 and Nd-doped Si–SiO_2 film sample D4 annealed to 700 °C for 457.9 nm excitation at 20 mW.

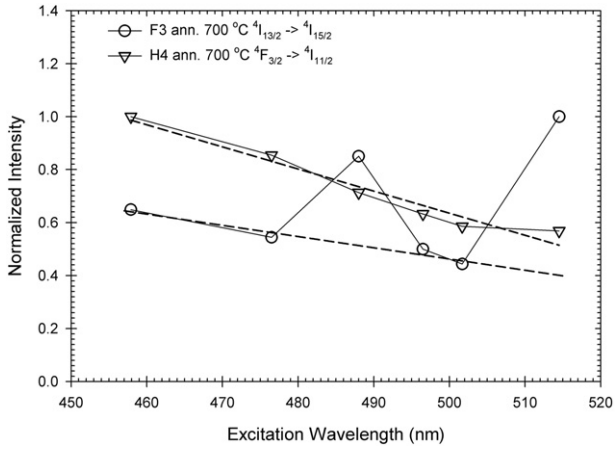

Figure 8. Excitation wavelength dependences for the 1527 nm emission intensity of Er-doped YSZ film sample F3 and the 1060 nm emission intensity of Nd-doped YSZ film sample H4, annealed to 700 °C for excitation power of 20 mW.

this emission is weaker for Nd-doped Si-rich SiO_2 films (see figure 7) [17, 29, 30]. So, Nd-doped Si-YSZ is a better candidate for optical amplifier applications in the O-band than Nd-doped Si–SiO_2, which seems to present more excited state absorption at the $^4I_{13/2}$ level and a smaller branching ratio for the $^4F_{3/2} \rightarrow {}^4I_{13/2}$ emission. No Tm^{3+}:$^3F_4 \rightarrow {}^3H_6$ emission was observed for J2 and J3. The $^3H_4 \rightarrow {}^3F_4$ relaxation does not seem to take place for these samples, which present then a predominant $^3H_4 \rightarrow {}^3H_6$ luminescent transition. The $^3F_4 \rightarrow {}^3H_6$ emission can be observed for Tm-doped Si-rich SiO_2 films for which it may appear to peak at 1650 nm [17] or at 1797 nm [29]. These peak wavelength values correspond to the U band in optical communications and obtaining a broad bandwidth at this range is important for applications in this field. This requires then a comparable branching ratio for the $^3H_4 \rightarrow {}^3F_4$ (non-radiative) transition with respect to the ratio for the $^3H_4 \rightarrow {}^3H_6$ luminescent transition. The lack of U band emission for J2 and J3 could be related to excitation migration among Tm^{3+} ions until a non-radiative defect is met [31], due to the high Tm concentration.

Figure 8 shows the Nd^{3+} : $^4F_{3/2} \rightarrow {}^4I_{13/2}$ and Er^{3+} : $^4I_{13/2} \rightarrow {}^4I_{15/2}$ emission excitation wavelength dependences for excitation power of 20 mW for film samples H4 and F3, respectively, annealed to 700 °C. The excitation wavelength dependence of the 1527 nm emission for F3 shows that the $^4I_{13/2} \rightarrow {}^4I_{15/2}$ emission is a result of the combination of the excitation due to energy transfer from defects in YSZ (from the C defects to the Er^{3+}:$^4F_{7/2}$ level for laser excitation at 488 nm or from the T defects to the Er^{3+}:$^2H_{11/2}$ level for laser excitation at 514.5 nm) with the excitation through energy transfer from Si np by the coupling between the Si=O surface states and the Er^{3+}:$^4I_{9/2}$ level [32] that takes place for all laser excitation wavelengths considered. In figure 8, for F3, the dotted line represents the emitted intensity generated by energy transfer from the Si np and the difference in intensity between the data points and the dotted lines for excitation wavelengths of 488.0 and 514.5 nm represent the emitted intensity generated by energy transfer from the respective defects in YSZ. The coupling between these defects and the

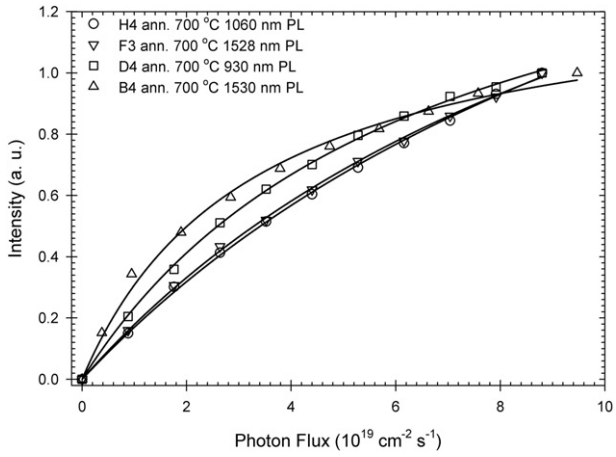

Figure 9. Excitation flux dependences for 1528 nm PL intensity of Er-doped YSZ film sample F3 for 488.0 nm excitation, 1060 nm PL intensity of Nd-doped YSZ film sample H4 for 457.9 nm excitation, 1530 nm PL intensity of Er-doped Si–SiO_2 film sample B4 for 457.9 nm excitation and 930 nm PL intensity of Nd-doped Si–SiO_2 film sample D4 for 457.9 nm excitation. Lines correspond to the rectangular hyperbolic fits to the data.

Er ions is quite strong, being strongest for the latter of the two excitation wavelengths, which corresponds to energy transfer from the F centers. This could be so due to relatively high absorption cross sections for the $^2H_{11/2}$ and the $^4S_{3/2}$ levels and also to the fact that, as the excitation wavelength increases, the availability of excitable Si nanoparticles decreases because the optical bandgaps increase with decrease in nanoparticle size [25, 33], so the excitation of Er^{3+} ions related to energy transfer from defects in YSZ must increase. In the case of H4, the Nd^{3+} : $^4F_{3/2}$ emissions are due to energy transfer from the Si np to the Nd^{3+}:($^4F_{5/2}$, $^2H_{9/2}$) levels, with no detectable transfer from defects in YSZ.

Figure 9 shows the excitation flux dependences for the 1528 nm emission intensity of film F3, for the 1060 nm emission intensity of film H4, and for comparison the 930 nm

emission intensity of film D4 as well as the 1530 nm emission intensity of Er-doped Si–SiO_2 film B4 (see table 1), all films annealed to 700 °C, for an excitation wavelength of 488 nm. The flux dependence is sub-linear for the photon flux range considered for all the films; saturation is not reached within this range: however, B4 is close to reaching saturation. Flux dependence is in the form of a rectangular hyperbola which can be expressed as $I = a\Phi/(1 + b\Phi)$ (I: normalized peak intensity of rare earth ion emission) with respect to the excitation flux (Φ), with coefficients a and b obtained by numerical fits to the data. By using an approximate two-level model for the Er^{3+}:$^4I_{13/2} \rightarrow {}^4I_{15/2}$ and Nd^{3+}:$^4F_{3/2} \rightarrow {}^4I_{11/2}$ emissions as presented either in [34] or in [17], applicable to rare-earth-doped dielectric or semiconductor hosts, the coefficient b would yield an approximate estimate of the product of the effective excitation cross section and the emission decay time. This product can give us a qualitative idea of the pumping efficiency of the films. A greater cross section as well as a slower decay should result in a greater pumping efficiency, so good emission intensity should be obtained with less excitation flux. The doped Si–SiO_2 samples present higher b values: (Er, B4) 0.31 and (Nd, D4) 0.15, than the doped Si-YSZ samples: (Er, F3) 0.08 and (Nd, H4) 0.07. The doped Si–SiO_2 films present a greater relative increase in intensity for lower photon flux values, though the difference is really appreciable for B4. The pumping efficiency of the Er^{3+}:$^4I_{13/2} \rightarrow {}^4I_{15/2}$ emission is greater than for the $^4F_{3/2} \rightarrow {}^4I_{j/2}$; $j = 9, 11, 13$ emissions, being most noticeable in doped Si–SiO_2 films. The difference is smaller for the doped Si-YSZ films due to the presence of energy transfer from defects in YSZ to the Er^{3+} ions. The difference in b values between the doped Si–SiO_2 films and the doped Si-YSZ can be related to the higher Si concentration and lower Er concentration in the former films. This should increase the relative probability for the rare earth ions of being excited by the Si nanoparticles by increasing their number without increasing their size beyond the limit where the Er^{3+}:$^4I_{9/2}$ and the Nd^{3+}:($^4F_{5/2}$, $^2H_{9/2}$) levels cease to become excited. The lower rare earth concentration of the doped Si–SiO_2 films should reduce the energy migration among rare earth ions. The doped Si-YSZ films, however, seem to accommodate high rare earth ion concentrations before concentration quenching of the IR emissions, especially in the case of Nd, as is shown in figure 7. The lower phonon energies for YSZ as compared with SiO_2 also reduce phonon-assisted non-radiative relaxation within the films. This, along with the strong coupling of the defects in YSZ and the Er ions for appropriate excitation wavelengths in the case of F3, would explain the relatively small ratios (2–4) between the respective b values for the doped Si–SiO_2 films and the doped Si-YSZ films.

An idea of the degree of energy migration among rare earth ions can be obtained for Er^{3+} ions by comparing the flux dependence of the $^4I_{11/2} \rightarrow {}^4I_{15/2}$ emission at 980 nm with that of the $^4I_{13/2} \rightarrow {}^4I_{15/2}$ emission at 1528 nm for Er-doped Si–SiO_2 and at 1530 nm for Er-doped Si-YSZ annealed to 700 °C. The comparisons for films F3 and B4 are shown in figure 10. The power law relation fitted to the data gives exponents of 1.4 and 1.3 for F3 and B4, respectively. In the case of F3 the

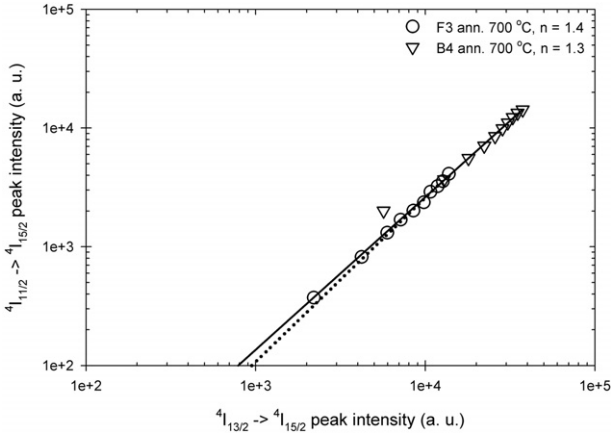

Figure 10. $^4I_{11/2} \rightarrow {}^4I_{15/2}$ PL peak intensity comparison with respect to the $^4I_{13/2} \rightarrow {}^4I_{15/2}$ PL peak intensity, for the Er-doped YSZ film sample F3 for 488.0 nm excitation and for the Er-doped Si–SiO_2 film sample B4 for 457.9 nm excitation, with an excitation power of 20 mW for both films. The lines correspond to power law fits to the data.

$^4I_{11/2} \rightarrow {}^4I_{15/2}$ emission can be a result of a combination of three excitation routes: one is related to the resonant excitation to the $^4F_{7/2}$ level (488 nm excitation) or the $^2H_{11/2}$ level (514.5 nm excitation) due to energy transfer from defects in YSZ, the next is a relaxation from the $^4I_{9/2}$ level to the $^4I_{11/2}$ level after energy transfer from Si np, and another is due to energy transfer upconversion (ETU) from one Er ion excited to the $^4I_{13/2}$ level to another Er ion also excited to the $^4I_{13/2}$ level. In the case of sample B4 population of the $^4I_{11/2}$ level can be through the branching from the $^4I_{9/2}$ level after energy transfer from the Si np or through the energy transfer upconversion (ETU) process involving neighboring Er ions. For both films the ETU processes, though significant, are not predominant and are balanced out by the branching processes. In the case of the Nd-doped films this method of comparison is not applicable. By ETU processes a Nd ion can undergo a relaxation from the $^4F_{3/2}$ level to the $^4I_{13/2}$ level and by energy transfer excite another nearby Nd ion from the $^4F_{3/2}$ level to the $^4G_{7/2}$ level, an ion that in turn would then relax non-radiatively to lower levels [21]. No emission is therefore detected and emission intensity comparisons are not possible even though ETU processes may be present. As the $^3H_4 \rightarrow {}^3H_6$ emission was the only emission detected for films J2 and J3 intensity comparisons were not possible to examine any ETU processes among Tm^{3+} ions: however, as mentioned before the lack of Tm^{3+}:$^3F_4 \rightarrow {}^3H_6$ emission could be an indicator of the degree of excitation migration among Tm^{3+} ions, due to the high Tm concentration.

The Si nanoparticles are located in the intermediate regions that separate the different crystalline grains from each other. The rare earth ions are located within the crystalline grains in substitutional positions. Those ions closest to the grain boundaries would mostly be excited by energy transfer from the Si nanoparticles. The ions located in the inner regions of the crystalline grains would be excited by energy migration among ions or by energy transfer from the defects within the grains. This would mostly be the case for Er, Nd and Tm ions with the Er ions being much more coupled with the defects

within the grains due to the greater availability of sites as the Er ions can be incorporated in sixfold, sevenfold and eightfold oxygen coordinated configuration sites. In the case of H3 and H4 there are a large number of small Si nanoparticles that can excite the Nd ions close to the grain boundaries and the solubility seems to be high. For H3 and H4 it seems that the majority of configuration sites are sevenfold oxygen-coordinated. The Tm-doped YSZ film J3 was amorphous, resulting in a more mixed distribution of Tm ions within the matrix and allowing for the coupling of the ions with the Si nanoparticles.

4. Conclusions

The RE-doped YSZ sputtered films prepared and annealed to 700 °C were mostly polycrystalline with crystalline ZrO_2 phases being predominant for Si content below ∼7.0 at.%. The low oxygen content in the films led to the presence of abundant oxygen-related defects which, along with cation-related vacancy defects, participate in the optical absorption and emission processes. PL in the visible was mainly defect-related due to excitation of higher defect levels in YSZ. Er^{3+} and Nd^{3+} PL detected in the visible upon 488.0 nm excitation was due to energy transfer from defects in YSZ. Tm^{3+} PL in the visible was due to energy transfer from Si nanoparticles. No Tm^{3+} IR PL was detected due to excitation migration among Tm^{3+} ions. The Er^{3+} IR PL was due to energy transfer from Si nanoparticles or defects in YSZ, or due to ETU processes among Er ions in the case of $^4I_{11/2} \rightarrow {}^4I_{15/2}$ emission. The Nd^{3+} IR PL was due only to energy transfer from Si nanoparticles. Pumping efficiency for Er- and Nd-doped YSZ is high, being close to that of Er- and Nd-doped Si–SiO_2. For Er- and Nd-doped YSZ the RE ions are located mostly at substitutional sites within the crystalline grains; the Si nanoparticles are located in the regions in between the grains and excite the rare earth ions closest to the grain boundaries while the inner ions can be excited either through energy transfer from the defects or by energy migration among the ions. For Tm-doped YSZ the ions can be more homogeneously distributed within the films. The high RE concentrations lead to a high degree of energy migration among (clustered) RE ions. RE IR emissions in Er-doped YSZ, Nd-doped YSZ and Tm-doped YSZ can be enhanced by reducing the RE pellet sizes and by increasing the oxygen content, making the films amorphous and increasing the chances of a better diffusion of the RE ions within the matrix.

In summary, we have studied Er-, Nd- and Tm-doped Si-rich YSZ composites to determine their spectroscopic properties motivated by the excellent qualities of zirconia as an optical material and the sensitizing effects of nanosilicon on the emission properties of RE-doped oxides. We have clarified the role of the silicon nanoparticles and defects on the excitation processes for each RE dopant and suggested procedures to increase emission intensities and bandwidths. The results presented show that these rare-earth-doped materials have good potential for photonic applications.

Acknowledgments

This work was supported by NASA under grant no. NCC3-1034, by NSF 0701525 and by UPR-FIPI.

References

[1] Harrison H D E, McLamed N T and Subbarao E C 1963 *J. Electrochem. Soc.* **110** 23
[2] De Vicente F S, De Castro A C, De Souza M F and Siu Li M 2002 *Thin Solid Films* **418** 222
[3] 2002 *MRS Bull.* **27** (whole of issue 3)
[4] Maeda N, Wada N, Onoda H, Maegawa A and Kojima K 2003 *Thin Solid Films* **445** 382
[5] Savoini B, Muñoz Santiuste J E and Gonzales R 1997 *Phys. Rev.* B **10** 5856
[6] Ramos-Brito F, García-Hipólito M, Martínez-Martínez R, Martínez-Sánchez E and Falcony C 2004 *J. Phys. D: Appl. Phys.* **37** L13
[7] Reisfeld R, Zelner M and Patra A 2000 *J. Alloys Compounds* **300/301** 147
[8] Pereyra-Perea E, Estrada-Yañez M R and García M 1998 *J. Phys. D: Appl. Phys.* **31** L7
[9] De la Rosa-Cruz E, Díaz-Torres L A, Salas P, Rodríguez R A, Kumar G A, Meneses M A, Mosiño J F, Hernández J M and Barbosa-García O 2003 *J. Appl. Phys.* **94** 3509
[10] De la Rosa-Cruz E, Díaz-Torres L A, Rodríguez-Rojas R A, Meneses-Nava M A, Barbosa-García O and Salas P 2003 *Appl. Phys. Lett.* **83** 4903
[11] Urlacher C, Marco de Lucas C, Bernstein E, Jacquier B and Mugnier J 1999 *Opt. Mater.* **12** 19
[12] Cross M and Varhue W 2004 *Mater. Res. Soc. Symp. Proc.* **789** N11.8
[13] French R H, Glass S J, Ohuchi F S, Xu Y–N and Ching W Y 1994 *Phys. Rev.* B **49** 5133
[14] Foster A S, Sulimov V B, López Gejo F, Shluger A L and Nieminen R M 2001 *Phys. Rev.* B **64** 224108
[15] Ostanin S and Salamatov E 2003 *Phys. Rev.* B **68** 172106
[16] Savoini B, Muñoz Santiuste J E and González R 1997 *Phys. Rev.* B **56** 5856
[17] Franzò G, Vinciguerra V and Priolo F 1999 *Appl. Phys.* A **69** 3
[18] Han H-S, Seo S-Y and Shin J H 2001 *Appl. Phys. Lett.* **79** 4568
[19] Kenyon A J, Loh W H, Oton C J and Ahmad I 2006 *J. Lumin.* **121** 193
[20] Priolo F, Franzó G, Pacifici D, Vinciguerra V, Iacona F and Irrera A 2001 *J. Appl. Phys.* **89** 264
[21] Becker P C, Olsson N A and Simpson J R 1999 *Erbium-Doped Amplifiers, Fundamentals and Technology* (San Diego, CA: Academic)
[22] Foster A S, Sulimov V B, López Gejo F, Shluger A L and Nieminen R M 2002 *J. Non-Cryst. Solids* **303** 101
[23] Orera V M, Merino R I, Chen Y, Cases R and Alonso P J 1990 *Phys. Rev.* B **42** 9782
[24] Petrik N G, Taylor D P and Orlando T M 1999 *J. Appl. Phys.* **85** 6770
[25] Wolkin M V, Jorne J, Fauchet P M, Allan G and Delerue C 1999 *Phys. Rev. Lett.* **82** 197
[26] Rozo C, Jaque D, Fonseca L F and García Solé J 2007 *J. Lumin.* **128** 1197
[27] Chen Y, Huang Y, Huang M, Chen R, Luo Z and Huang M 2005 *J. Am. Ceram. Soc.* **88** 19
[28] Bouderbala M, Mohmoh H, Bahtat A, Bahtat M, Ouchetto M, Druetta M and Elouadi B 1999 *J. Non-Cryst. Solids* **259** 23
[29] Watanabe K, Tamaoka H, Fujii M, Moriwaki K and Hayashi S 2002 *Physica* E **13** 1038
[30] Seo S-Y, Kim M-J and Shin J H 2000 *Appl. Phys. Lett.* **83** 2778
[31] Polman A 1997 *J. Appl. Phys.* **82** 1
[32] Franzò G, Pacifici D, Vinciguerra V, Priolo F and Iacona F 2000 *Appl. Phys. Lett.* **76** 2167
[33] Allan G, Delerue C and Lannoo M 1997 *Phys. Rev. Lett.* **78** 3161
[34] Gusev O B, Bresler M S, Pak P E, Yassievich I N, Forcales M, Vinh N Q and Gregorkiewicz T 2001 *Phys. Rev.* B **64** 75302